The formation and stability of Petschek reconnection

H. Baty, T. G. Forbes, and E. R. Priest

Citation: Physics of Plasmas (1994-present) **21**, 112111 (2014); doi: 10.1063/1.4901918
View online: http://dx.doi.org/10.1063/1.4901918
View Table of Contents: http://scitation.aip.org/content/aip/journal/pop/21/11?ver=pdfcov
Published by the AIP Publishing

The formation and stability of Petschek reconnection

H. Baty,[1,a)] T. G. Forbes,[2,b)] and E. R. Priest[3,c)]
[1]*Observatoire Astronomique de Strasbourg, Université de Strasbourg, CNRS, UMR 7550, 11 rue de l'Université, F-67000 Strasbourg, France*
[2]*Institute for the Study of Earth, Oceans, and Space, University of New Hampshire, Durham, New Hampshire 03824, USA*
[3]*Institute of Mathematics, University of St. Andrews, Fife KY169SS, Scotland, United Kingdom*

(Received 18 September 2014; accepted 4 November 2014; published online 19 November 2014)

A combined analytical and numerical study of magnetic reconnection in two-dimensional resistive magnetohydrodynamics is carried out by using different explicit spatial variations of the resistivity. A special emphasis on the existence of stable/unstable Petschek's solutions is taken, comparing with the recent analytical model given by Forbes *et al.* [Phys. Plasmas **20**, 052902 (2013)]. Our results show good quantitative agreement between the analytical theory and the numerical solutions for a Petschek-type solution to within an accuracy of about 10% or better. Our simulations also show that if the resistivity profile is relatively flat near the *X*-point, one of two possible asymmetric solutions will occur. Which solution occurs depends on small random perturbations of the initial conditions. The existence of two possible asymmetric solutions, in a system which is otherwise symmetric, constitutes an example of spontaneous symmetry breaking. © *2014 AIP Publishing LLC*.
[http://dx.doi.org/10.1063/1.4901918]

I. INTRODUCTION

Magnetic reconnection is a fundamental process in astrophysical and laboratory plasmas, where a change of magnetic field line connectivity allows the conversion of magnetic energy into kinetic and fast particle energy. For example, it is widely accepted that magnetic reconnection plays a crucial role for observed fast energy release and associated particle acceleration in solar flares (see Ref. 1 and references therein). The classical model of reconnection is based on Sweet-Parker theory in the two-dimensional (2D) resistive magnetohydrodynamics (MHD) framework, in which a steady-state current sheet structure with a small central diffusion layer controls the reconnection between two regions of oppositely directed magnetic fields.[2,3] However, the Sweet-Parker (SP) model gives a reconnection rate too small to explain the fast time scales of solar flares or laboratory plasma disruptions.

A considerable amount of work has also been devoted to an alternative reconnection model, initially introduced by Petschek.[4] Petschek's model was thought to provide a universal fast reconnection mechanism thanks to the formation of four standing slow-mode shocks surrounding a very small central diffusion region. However, it was progressively realized that Petschek reconnection is generated only when specific conditions are satisfied, most of which depend on the spatial dependence of the resistivity.

After years of debate on the latter puzzling aspect, a recent theoretical analysis has helped to clarify the situation.[5] The new analysis shows that Petschek solutions are structurally unstable when the resistivity is uniform. This inherent instability also explains why Sweet-Parker solutions are the only stable steady-state solutions seen in simulations with uniform resistivity. The situation is different when a nonuniform resistivity profile is employed. In this case, a stable steady-state Petschek solution may occur if the resistivity profile is suitably shaped. For symmetric configurations, a suitably shaped profile is one in which the resistivity decreases with the square of the distance near the *X*-point. A symmetric resistivity profile that increases with distance from the *X*-point or is relatively flat is predicted not to generate a stable symmetric solution. However, as we show here, such profiles may generate asymmetric solutions that are both Petschek like and stable.

The aim of the present work is to address the validity of the predictions made by the recent theoretical analysis of Forbes *et al.*,[5] by carrying out time-dependent simulations with the full set of two-dimensional resistive MHD equations. More precisely, we investigate the formation and stability of Petschek reconnection by prescribing different spatial variations for the resistivity profile.

The organization of the paper is as follows. In Sec. II, we present the governing equations and numerical setup. In Sec. III, we expand the previously published analytical theory[5] to allow for asymmetry and compressibility. The simulations results are presented in Sec. IV. Finally, we end with a discussion and conclusion in Sec. V.

II. NUMERICAL MODEL AND INITIAL SETUP

We solve the standard set of compressible resistive MHD equations (viscosity and thermal conductivity are ignored) written in the following dimensionless form:

$$\frac{\partial \rho}{\partial t} + \nabla \cdot (\rho \mathbf{v}) = 0, \tag{1}$$

$$\frac{\partial \rho \mathbf{v}}{\partial t} + \nabla \cdot \left(\rho \mathbf{v}\mathbf{v}^T + p_{tot}\mathbf{I} - \mathbf{B}\mathbf{B}^T\right) = \mathbf{0}, \tag{2}$$

a)Electronic mail: hubert.baty@unistra.fr.
b)Electronic mail: terry.forbes@unh.edu.
c)Electronic mail: eric@mcs.st-and.ac.uk.

$$\frac{\partial \mathbf{B}}{\partial t} + \nabla \cdot (\mathbf{v}\mathbf{B}^T - \mathbf{B}\mathbf{v}^T) = -\nabla \times (\eta \mathbf{J}), \quad (3)$$

$$\frac{\partial e}{\partial t} + \nabla \cdot \left(e\mathbf{v} + p_{tot}\mathbf{v} - \mathbf{v} \cdot \mathbf{B}\mathbf{B}^T\right) = \eta \mathbf{J}^2 - \mathbf{B} \cdot \nabla \times (\eta \mathbf{J}), \quad (4)$$

$$\mathbf{J} = \nabla \times \mathbf{B}, \quad (5)$$

$$\nabla \cdot \mathbf{B} = 0. \quad (6)$$

Here, ρ is the plasma density, p is the thermal pressure, $\mathbf{v}$ is the fluid velocity, $\mathbf{B}$ is the magnetic fluid, and $\mathbf{J}$ is the electrical current density. The total pressure (thermal + magnetic) is defined as $p_{tot} = p + B^2/2$, and the total energy density is $e = \rho v^2/2 + B^2/2 + p/(\gamma - 1)$, where γ is the ratio of specific heats. $\mathbf{I}$ is the identity tensor. Note that the magnetic permeability is taken to be unity.

We assume a Harris current sheet configuration (see Fig. 1), with a magnetic field parallel to the y-axis and varying with x,

$$B_x = 0; \quad B_y = B_e \tanh(x/a), \quad (7)$$

where B_e is the amplitude of the field and a is the initial half-width of the current layer. We set the ratio of specific heats γ equal to 5/3. We set $B_e = 1$ and $a = 0.1$, to define our normalization. A static equilibrium is considered with force balance provided by the plasma density variation in an isothermal medium

$$T = \beta/2, \quad \rho(x) = \frac{1 + \beta - B_y^2(x)}{\beta}, \quad (8)$$

where T and ρ are the temperature and plasma density, respectively. Note that the β parameter is the plasma-β taken at the outer x-boundary, and represents an upstream β parameter in this work. To determine the effects of compressibility, we consider $\beta = 0.35$ and $\beta = 10.0$.

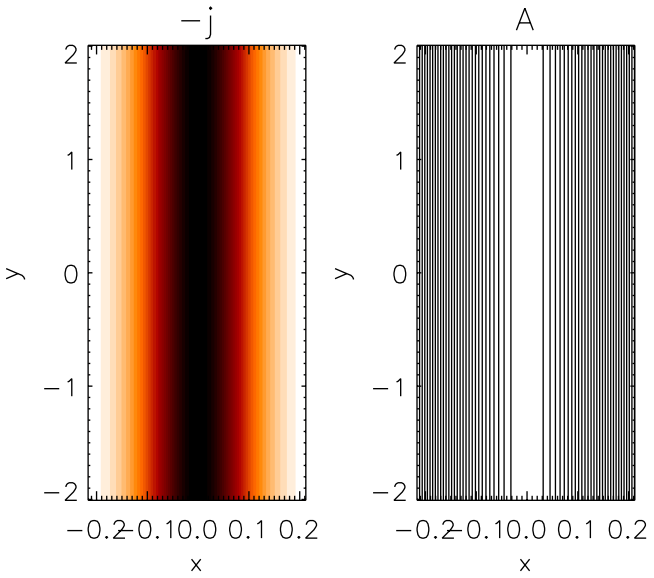

FIG. 1. Current density J (left panel) and magnetic field lines (right panel) for the initial equilibrium state. Only the central part of the full simulation domain is shown with x values in the range [−0.2: 0.2].

In this work, a total of 400×800 spatial grid points is used in the spatial domain $-L_x \le x \le L_x$ and $-L_y \le y \le L_y$, of dimensions $L_x = 1$ and $L_y = 2$. The time is normalized with respect to the Alfvén transit time t_A across the half-width computational box. A nonuniform spacing with a grid accumulation in the x direction is chosen in order to have sufficient cells to resolve the central current layer. Typically, we are able to achieve a minimum grid spacing of $\Delta x = 1 \times 10^{-3}$ in the x direction, together with a uniform spacing of $\Delta y = 5 \times 10^{-3}$ in y direction.

We use the general finite-volume based Versatile Advection Code (VAC),[6] and select the explicit one-step total variation diminishing (TVD) scheme with minmod limiting.[7,8] This is a second-order accurate shock-capturing method making use of a Roe-type approximate Riemann solver. To handle the solenoidal constraint on the magnetic field (Eq. (6)), our VAC simulations apply a projection scheme at every time step in order to remove any numerically generated divergence of the magnetic field up to a predefined accuracy.[9]

The boundary conditions are imposed through the use of two ghost cells located slightly outside the computational domain at each boundary. Following Refs. 10–12, we overspecify boundary conditions at the inflow boundary $x = \pm L_x$ (with respect to the required conditions). More precisely, five conditions are imposed on five physical quantities to be fixed in time and equal to their initial values, namely, the mass density, two components of the flow velocity, the y component of the magnetic field, and the total energy density. In this way, the system is free to choose its own reconnection solution without being driven by external forcing, as expected for Petschek solutions.[13] For more details, the reader can refer to the discussion in Sec. III of Ref. 10 and references therein. Additionally, free conditions are imposed at the outflow boundaries $y = \pm L_y$, by prescribing zero normal derivatives on the different physical quantities as detailed in Refs. 11 and 12.

In order to obtain Petschek solutions numerically, we follow a classical procedure by starting from the initial Harris equilibrium (given by Eq. (7)), and apply the following Gaussian spatial variation for the resistivity coefficient:

$$\eta(x, y) = \eta_0 \exp[-(x/l_x)^2 - (y/l_y)^2], \quad (9)$$

where η_0 is the resistivity at the centre of the domain, and l_x and l_y are the characteristic length scales of the spatial resistivity variation. This setup allows us to achieve Sweet-Parker-like solutions when large values of l_y (close to the domain dimension L_y) are employed,[14] and Petschek solutions for small l_y values, $l_y \ll L_y$.[10–12] Along the transverse direction, l_x is fixed to $l_x = 0.05$ and does not influence our results as long as it is larger than the width of the central diffusion region. The evolution of the system is thus followed for different runs corresponding to different resistivity l_y values. In most of the present study, unless specifically written, a fixed value of η_0 is taken, with $\eta_0 = 5 \times 10^{-4}$.

The other resistivity profile that we will consider is the non-Gaussian one proposed by Forbes *et al.*[5]

$$\eta(x,y) = \eta_0 \exp[-(x/l_x)^2 - (y/l_y)^4], \tag{10}$$

which has the same x-variation, but decreases more rapidly for $y > l_y$. They predict that this profile will not have a stable, symmetric solution because it is too flat near the X-line. However, they did not consider the possibility that there might be asymmetric solutions.

III. ANALYTICAL TREATMENT

Earlier work by Vasyliunas,[15] Titov,[16] and Somov,[17] forms the basis for the recent analysis by Forbes *et al.*[5] These authors reduce the two-dimensional reconnection problem to a one-dimensional one by first expanding the equations in terms of the inflow Alfvén Mach number, M_A, and then averaging over the current layer that consists of the diffusion region and slow-mode shocks (cf. Fig. 2). The simplified equations that result are similar to the one-dimensional MHD nozzle equations that are often used to describe the flow of magnetized plasma in astrophysical jets.[18–20] A similar approach has also been used by Malyshkin *et al.* and by Kulsrud.[21,22]

Since a detailed derivation of the averaged one-dimensional equations has already been published,[17,23] we start with these equations and then show how to find stable, asymmetrical, solutions. Using the same notation and normalization as Eqs. (1)–(6), the averaged equations are as follows:

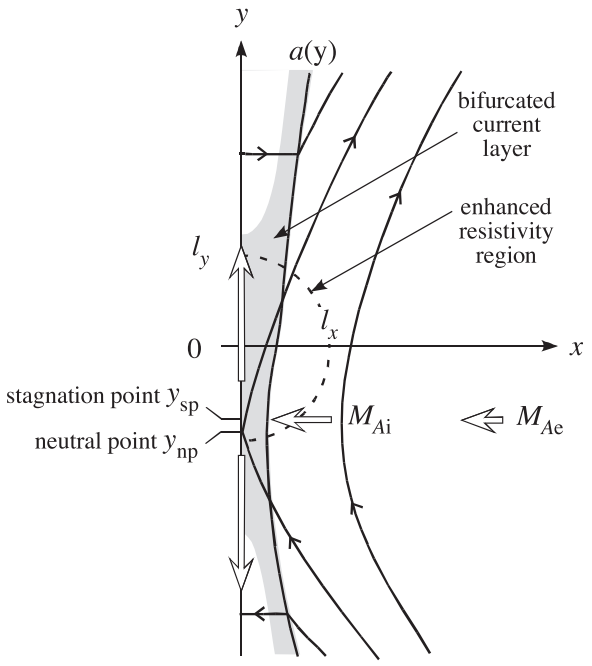

FIG. 2. Diagram showing the orientation of the current layer relative to the coordinate system. The gray shaded region corresponds to the region of high current density. Solid curves denote magnetic field lines, while white arrows indicate the flows into and out of the stagnation point at y_{sp}. In the inflow region the Alfvén Mach number increases from M_{Ae} (external value) to M_{Ai} (internal value) as the plasma flows towards the stagnation point. When the solution is asymmetric, the x-line at y_{np} (np for neutral point) is not necessarily co-located with the stagnation point at y_{sp}. The curve labeled $a(y)$ is the half thickness of the current layer, which includes both the diffusion region and the slow-mode shocks. The dashed curve indicates the region of locally enhanced resistivity.

$$\partial(a\langle\rho\rangle\langle v_y\rangle)/\partial y = -\rho_a v_{xa}, \tag{11}$$

$$\partial(\langle\rho\rangle\langle v_y\rangle^2 a)/\partial y = -a\partial\langle p\rangle/\partial y + B_{ya}\langle B_x\rangle, \tag{12}$$

$$\langle p\rangle = B_{ya}^2/2 + p_a, \tag{13}$$

$$E_a = M_{Ai} = -B_{ya}v_{xa} = \langle v_y\rangle\langle B_x\rangle + \eta B_{ya}/a, \tag{14}$$

$$\partial\{[\langle\rho\rangle\langle v_y\rangle^2/2 + \gamma\langle p\rangle/(\gamma-1)]a\langle v_y\rangle\}/\partial y = -[\gamma p_a/(\gamma-1) + B_{ya}^2]v_{xa}, \tag{15}$$

$$B_{xa} = \langle B_x\rangle + B_{ya}\partial a/\partial y. \tag{16}$$

Here, E is the electric field and M_{Ai} is the Alfvén Mach number of the inflowing plasma at $x = a$, $y = y_{sp}$, immediately upstream of the current layer at the location of the stagnation point as shown in Fig. 2. The a subscripts indicate quantities evaluated at $x = a$, while the brackets $\langle\rangle$ indicate averages of the form

$$\langle v_y\rangle = (1/a)\int_0^a v_y(x,y)dx. \tag{17}$$

Several key assumptions are made in obtaining Eqs. (11)–(16). First, the Alfvén Mach number, M_{Ai}, is assumed to be much less than one. This assumption means that a, v_x, and B_x are small (of order M_{Ai}). Second, v_{ya}, the external flow parallel to the current layer is assumed to be negligible (of order M_{Ai}^2 or smaller). This particular assumption is valid for Petschek reconnection, but not for other types of reconnection such as flux pile up.[24] Third, ρ, v_y, and B_x are assumed to be nearly uniform in x within the current layer, so that averages of a product like $\langle\rho v\rangle$, can be approximated by the product of its averages, $\langle\rho\rangle\langle v\rangle$. Finally, B_y within the current layer is assumed to be of order M_{Ai}^1 or smaller, so that $\langle B_y\rangle$ is negligible. This last assumption is reasonable for the slow-shock region, but it is somewhat questionable for the diffusion region where B_y is expected to be of order M_{Ai}^0 near the X-point. Forbes *et al.* estimate that neglecting $\langle B_y\rangle$ introduces an error of less than 10% in the calculation of the reconnection rate.[5]

The quantities ρ_a, p_a, and B_{ya} that appear in Eqs. (11)–(16) are determined by the external density, pressure, and field outside the current layer. For undriven reconnection ρ_a and p_a are uniform to order M_{Ai}^1, so they can be treated as constants in a first-order analysis.[24] The variation of B_{ya}, however, depends on the specific assumptions made about the external field configuration. In the original treatment by Petschek[4] and the subsequent treatment by Vasyliunas,[15] B_{ya} is assumed to be uniform to lowest order (M_{Ai}^0). However, in the treatments by Titov,[16] Somov,[17] and Malyshkin and Kulsrud,[25] B_{ya} is assumed to vary as $\sqrt{L_y^2 - y^2}$ to lowest order, where L_y is the global scale length. This variation corresponds to the solutions of Green[26] and Syrovatskii[27] for the field near an infinitely thin current sheet.

As discussed in Forbes *et al.*,[5] the nonuniformity of B_{ya} plays nearly the same role as the nonuniformity of η in determining the reconnection rate. If η is uniform, then the length of the diffusion region is roughly the same as L_y, and the reconnection is of Sweet-Parker type. On the other hand, if η

is nonuniform and varies over a scale $l_y \ll L_y$, then the reconnection is of Petschek type. Since all of the solutions we consider satisfy this latter condition reasonably well ($l_y/L_y = 0.15$), we will, for simplicity, ignore the variation of B_{ya} and set $B_{ya} = 1$. One consequence of this assumption, which follows from Eqs. (12) and (13), is that the stagnation point, y_{sp}, and neutral point, y_{np}, are approximately co-located when $\partial B_{ya}/\partial y = 0$.

With our normalization $\rho_a = 1$ and $p_a = \beta/2$ where β is the plasma beta upstream of the current layer, and Eqs. (11)–(15) combine to give the following ordinary differential equation for $\langle v_y \rangle$:

$$\langle v_y \rangle + (y - y_{sp})\partial \langle v_y \rangle / \partial y = 1/\langle v_y \rangle - 5\alpha(\eta(y)/\eta_c)\langle \rho \rangle / (y - y_{sp}), \tag{18}$$

where

$$\langle \rho \rangle = 5(1+\beta)/(5\beta + 4 - 2\langle v_y \rangle^2), \tag{19}$$

$\alpha = \eta_c / M_{Ai}^2$, $\eta_c = \eta(0)$, and $\gamma = 5/3$. In the incompressible Sweet-Parker theory, the parameter α corresponds to the length of the diffusion region.[3] In our compressible analysis, $|y| < \alpha$ is roughly the location where the diffusive electric field, $\eta B_{ya}/a$, dominates over the advective electric field, $\langle v_y \rangle \langle B_x \rangle$, in (14). In the limit of $\beta \to \infty$, (18) reduces to the incompressible equation obtained by Vasyliunas.[15] Equation (18) is the same as the compressible equation obtained by Somov and by Titov when $|y| \ll L_y$.[16,17] In addition to (18) and (19), we have the auxiliary equations

$$a = M_{Ai}(y - y_{sp})/\langle \rho \rangle \langle v_y \rangle, \tag{20}$$

$$\langle B_x \rangle = (M_{Ai} - \eta/a)/\langle v_y \rangle, \tag{21}$$

for the thickness, a, and averaged transverse field, B_x, of the current layer. As $y \to \infty$, $v_y \to 1$ (i.e., the Alfvén speed), and the density predicted by (19) reduces to that predicted by the standard jump conditions for a switch-off slow-mode shock. Also in this limit the averaged transverse field $\langle B_x \rangle$ given by (21) is equal to M_{Ai}, just as it is in Petschek's theory.[4]

A principal finding of the previous analysis by Forbes *et al.* is that most solutions of (18) are structurally unstable due to an essential singularity at the stagnation point, y_{sp}.[5] Although $\langle v_y \rangle$ is zero at this point, its higher-order derivatives are not well behaved there. In the time-dependent system of equations considered by Forbes *et al.*, the singular solutions rapidly decay at the Alfvén time-scale when approximated by a smoothed, nonsingular function.[5]

Not all solutions of (18) are necessarily singular. When either η or B_{ya} is nonuniform, one or more nonsingular solutions may exist, and these nonsingular solutions are stable. In fact they act as fixed-point attractors in the time-dependent system.[5] A key property that distinguishes the nonsingular solutions from the singular ones is that the nonsingular solutions are analytic at y_{sp}, while the singular ones are not. In real analysis, a function that is analytic at a particular point is exactly equal to its Taylor expansion around that point within a nonzero domain. Therefore, we can determine the conditions needed for a structurally stable solution by expanding $\langle v_y(y) \rangle$ and $\eta(y)$ around y_{sp} as follows:

$$\langle v_y \rangle = V_1(y - y_{sp}) + V_2(y - y_{sp})^2 + V_3(y - y_{sp})^3 + \cdots, \tag{22}$$

$$\eta(y) = \eta_0 + \eta_1(y - y_{sp}) + \eta_2(y - y_{sp})^2 + \eta_3(y - y_{sp})^3 + \cdots, \tag{23}$$

where the coefficients V_i and η_i are functions of both α and y_{sp}. A sufficient condition for the convergence of the series for $\langle v_y \rangle$ at y_{sp} is that

$$\lim_{n \to \infty} V_n = 0. \tag{24}$$

Accurate approximations of the values of α and y_{sp} that satisfy (24) can be determined by using the high-order coefficients in the expansion. To show how this works, we substitute the power series (22) and (23) into (18) and obtain

$$V_1 = \frac{4 + 5\beta}{5\alpha(1+\beta)} \frac{\eta_c}{\eta_0}, \tag{25}$$

$$V_2 = -\frac{(4 + 5\beta)\eta_c \eta_1}{5\alpha(1+\beta)\eta_0^2}, \tag{26}$$

$$V_3 = \frac{(4 + 5\beta)\eta_c}{25\alpha^3(1+\beta)^2\eta_0^3}[-2(4 + 5\beta)\eta_c^2 + 5\alpha^2(1+\beta)(\eta_1^2 - \eta_0\eta_2)], \tag{27}$$

$$V_4 = \frac{(4 + 5\beta)\eta_c}{125\alpha^3(1+\beta)^3\eta_0^4}[25\alpha^2(1+\beta)^2(-\eta_1^3 + 2\eta_0\eta_1\eta_2 - \eta_0^2\eta_3) + (4 + 5\beta)(34 + 35\beta)\eta_c^2\eta_1], \tag{28}$$

for the first four coefficients of the series. Setting $V_3 = 0$ and $V_4 = 0$ give two equations that approximately determine the values of α and y_{sp} of the nonsingular solutions provided that the series converges. These two equations are

$$5\alpha^2(1+\beta)(\eta_1^2 - \eta_0\eta_2) = 2(4 + 5\beta)\eta_c^2, \tag{29}$$

and

$$25\alpha^2(1+\beta)^2(-\eta_1^3 + 2\eta_0\eta_1\eta_2 - \eta_0^2\eta_3) = -(4 + 5\beta)(34 + 35\beta)\eta_1\eta_c^2. \tag{30}$$

Let us first consider the specific case of the Gaussian profile $\eta = \eta_c e^{-y^2/l_y^2}$. The first four coefficients of its series expansion are then

$$\eta_0 = \eta_c e^{-y_{sp}^2/l_y^2},$$

$$\eta_1 = -2(y_{sp}/l_y^2)\eta_c e^{-y_{sp}^2/l_y^2},$$

$$\eta_2 = (1/l_y^4)(2y_{sp}^2 - l_y^2)\eta_c e^{-y_{sp}^2/l_y^2},$$

$$\eta_3 = 2(y_{sp}/l_y^6)(l_y^2 - 2y_{sp}^2/3)\eta_c e^{-y_{sp}^2/l_y^2}.$$

Substitution of these coefficients into (29) and (30) yields

$$y_{sp} = 0, \tag{31}$$

$$\alpha \approx [2(4+5\beta)/5(1+\beta)]^{1/2} l_y, \tag{32}$$

$$M_{Ai} = \sqrt{\eta_c/\alpha}, \tag{33}$$

with

$$M_{Ai} \approx \sqrt{\eta_c/l_y}[5(1+\beta)/2(4+5\beta)]^{1/4}. \tag{34}$$

Equation (34) is the lowest order approximation for the reconnection rate M_{Ai}, but only if the series for $\langle v_y \rangle$ converges. In Sec. IV, we discuss a more complex example where (34) has a reasonable looking solution, but the series fails to converge because its higher-order coefficients are not well behaved.

If the series does converge, then more accurate, but more complicated expressions can be obtained by setting progressively higher coefficients of the expansion of $\langle v_y \rangle$ to zero. To determine and manipulate these more complicated expressions, we use the software *Mathematica*. The higher order coefficients generate multiple roots, and it is the smallest, positive root that corresponds to the stable solution. Table I shows the approximate values of M_{Ai} obtained in this way for the Gaussian profile. This table assumes $\eta = 5 \times 10^{-4}$ and $l_y = 0.3$, the same values as used in our simulations.

From the table, we see that the approximate values of M_{Ai} rapidly converge as increasing higher-order coefficients are used. By $V_{11} = 0$, the value of M_{Ai} corresponding to a stable solution has been determined to six significant figures. This level of accuracy does not mean that we have calculated the actual reconnection rate to a similar level. The one-dimensional averaged equations that we use are highly idealized, and we do not expect them to be any more accurate than the one-dimensional nozzle equations that they resemble. The one-dimensional nozzle equations typically have errors on the order of 10%–20% due to the fact that they ignore (as we do here) variations in the fluid variables across the width of the nozzle.[28] Table I also shows that the dependence of the reconnection rate on the plasma β is weak. Even when one compares the extreme cases of $\beta = 0$ (strong magnetic field limit) and $\beta \to \infty$ (incompressible limit), M_{Ai} only changes by about 6%.

Let us now consider the non-Gaussian profile $\eta = \eta_c e^{-y^4/l_y^4}$. One of the predictions of the previous analysis is that no stable, symmetric solution exists for this η profile. The first four coefficients of its expansion are

$$\eta_0 = \eta_c e^{-y_{sp}^4/l_y^4},$$
$$\eta_1 = -4(y_{sp}^3/l_y^4)\eta_c e^{-y_{sp}^4/l_y^4},$$
$$\eta_2 = (2y_{sp}^2/l_y^8)(4y_{sp}^4 - 3l_y^4)\eta_c e^{-y_{sp}^4/l_y^4},$$
$$\eta_3 = 4(y_{sp}/l_y^{12})(-l_y^8 + 6y_{sp}^4 l_y 4 - 8y_{sp}^8/3)\eta_c e^{-y_{sp}^4/l_y^4}.$$

We see right away that if $y_{sp} = 0$, as it must for a symmetric solution, then the three coefficients η_1, η_2, and η_3 are all zero, and, consequently, there is no real solution to Eq. (24) that has $y_{sp} = 0$. Any solutions that do exist must, therefore, be asymmetric. Substitution of the non-Gaussian η coefficients into (29) and (30) does actually yield two such solutions, namely,

$$y_{sp} \approx \pm l_y \sqrt[4]{\frac{-216 - 225\beta + \sqrt{68736 + 142080\beta + 73425\beta^2}}{8(92+95\beta)}}, \tag{35}$$

$$\alpha \approx \frac{l_y^4}{y_{sp}} \sqrt{\frac{4+5\beta}{5(1+\beta)(3l_y^4 + 4y_{sp}^4)}} e^{y_{sp}^4/l_y^4}. \tag{36}$$

Substitution of (36) into (33) gives the corresponding reconnection rate

$$M_{Ai} \approx \sqrt{\frac{\eta_c y_{sp}}{l_y^4} e^{-y_{sp}^4/l_y^4} \sqrt{\frac{5(1+\beta)(3l_y^4 + 4y_{sp}^4)}{(4+5\beta)}}}. \tag{37}$$

The two solutions have stagnation points located on opposite sides of the origin, but both have the same rate of reconnection. Only one of these solutions can occur at any given time. Since the resistivity profile is still symmetric, the theory predicts that the symmetry of the system will be spontaneously broken. As we will see in Sec. IV, the MHD simulations do, in fact, exhibit this behavior.

For $\eta = 5 \times 10^{-4}$, $l_y = 0.3$, and $\beta = 0.35$, Eqs. (35) and (37) give $y_{sp} = \pm 0.14978$ and $M_{Ai} = 0.039078$. Equations (35) and (37) constitute the lowest-order approximations for the location of the stagnation point y_{sp} and the reconnection rate M_{Ai}. As before, more accurate approximations are obtained by setting progressively higher coefficients of the expansion of $\langle v_y \rangle$ to zero as shown in Table II. Again, values in the table are for the simulation values of $\eta = 5 \times 10^{-4}$ and $l_y = 0.3$.

We will compare the highest-order approximations obtained using $V_{11} = 0$ and $V_{12} = 0$ to the simulation results in Sec. IV.

TABLE I. Reconnection rate at different levels of approximation for the Gaussian profile.

Approximation level	M_{Ai}, $\beta = 0.35$	M_{Ai}, $\beta = 10$
$V_3 = 0$	0.035734	0.034487
$V_5 = 0$	0.036980	0.035997
$V_7 = 0$	0.037033	0.036090
$V_9 = 0$	0.037034	0.036094
$V_{11} = 0$	0.037034	0.036094

TABLE II. Reconnection rate and stagnation point location at different levels of approximation for the non-Gaussian profile, for $\beta = 0.35$.

Approximation level	M_{Ai}	y_{sp}
$V_3 = 0, V_4 = 0$	0.039078	± 0.14978
$V_5 = 0, V_6 = 0$	0.040340	± 0.15069
$V_7 = 0, V_8 = 0$	0.040349	± 0.15208
$V_9 = 0, V_{10} = 0$	0.040352	± 0.15228
$V_{11} = 0, V_{12} = 0$	0.040352	± 0.15228

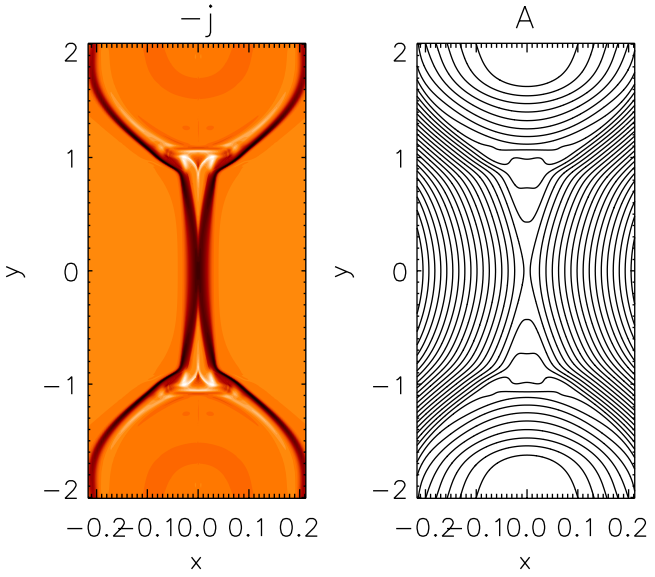

FIG. 3. Current density J (left panel) and magnetic field lines (right panel) corresponding to a transient state (at $t = 13$) for a simulation using $l_y = 0.3$ and a Gaussian resistivity profile.

IV. RESULTS OF COMPUTATIONAL EXPERIMENTS

A. Petschek solutions for Gaussian resistivity profiles

The appearance of a typical Petschek solution may be described as follows for $l_y = 0.3$. After a transient phase (see Fig. 3, and described in detail elsewhere[10,29]), a steady-state reconnection solution develops as seen in Fig. 4. This final steady-state has all the features of a Petschek solution, with a small central diffusion region surrounded by four standing shocks (slow mode MHD waves). The details have been already reported and characterized several times in analytical and numerical studies.[29–31]

Fig. 5 compares the steady-state outflow velocity from the numerical simulation shown in Fig. 4 with the prediction of the analytical theory. Since the theory only predicts an averaged velocity, the simulations results have been averaged across the

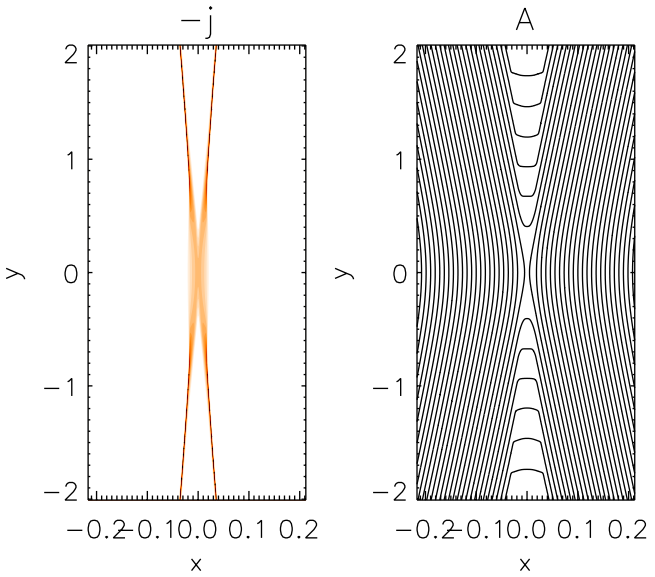

FIG. 4. Same as in Fig. 3 for the final steady state obtained at $t = 40$.

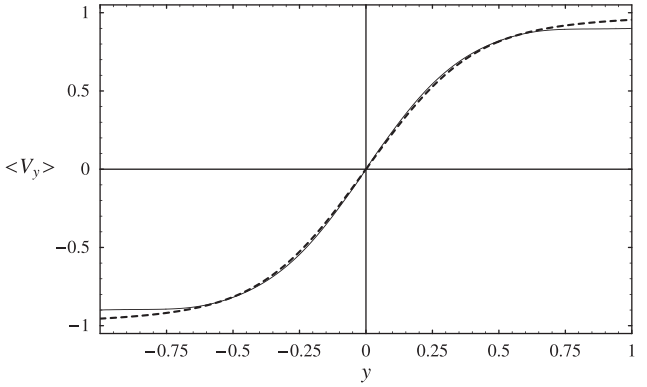

FIG. 5. Comparison of the averaged outflow velocity, $\langle v_y \rangle$ from the numerical simulation using a Gaussian resistivity profile (solid curve) with the corresponding flow predicted by the analytical theory (dashed curve). The simulation curve is for the time shown in Fig. 4, and the flows are normalized to the Alfvén speed. The good agreement between the two curves is remarkable considering that there are no free parameters in the theory that can be arbitrarily adjusted.

thickness of the outflow layer. The numerical averaging uses the half-maximum of v_y to locate the edge of the outflow layer. As shown in the first line of Table III, the difference between the numerical and analytical reconnection rates is about 5%. The simulation and theory curves are nearly identical within the diffusion region, but they show a slight divergence from one another in the region $|y| > 0.7$. This divergence is most likely due to the fact that the simplified version of the theory that we use here ignores the variation of the exterior tangential field, $B_y(a, y)$, with y. This field component decreases with y, which causes a slight decrease in the outflow speed because of the decrease in the exterior Alfvén speed with distance.[17]

The second line of Table III shows that varying the plasma β has a relatively small effect on the reconnection rate. In the simulation, the reconnection increases by about 10%, while the theory predicts it should decrease by about 2%. A possible explanation for this discrepancy is that the theory's assumption that ρ and v_y have little variation in x within the flow layer becomes increasingly problematical as the plasma β decreases. This difficulty is illustrated in Fig. 6, which compares the density for two different simulation runs with $\beta = 0.5$ and $\beta = 2.0$ after a steady state has been achieved.

Fig. 6 shows that there is a thin, low-density layer that is embedded within the thicker outflow region. The density reduction is most pronounced within the diffusion region. The high β case has less variation in density because it becomes more difficult to compress or expand the fluid as the magnetic field weakens relative to the gas pressure. Similar reduced density layers can also be seen in other simulations (see Fig. 7 in Yokoyama and Shibata, for

TABLE III. Comparison of numerical and analytical reconnection rates (M_{Ai}).

η profile	β	Simulation	Theory	Difference (%)
Gaussian	0.35	0.0353	0.037	+4.9
Gaussian	10	0.039	0.0361	−7.5
Non-Gauss.	0.35	0.0355	0.0403	+13.7
Non-Gauss.	10	0.039	0.0392	+0.5

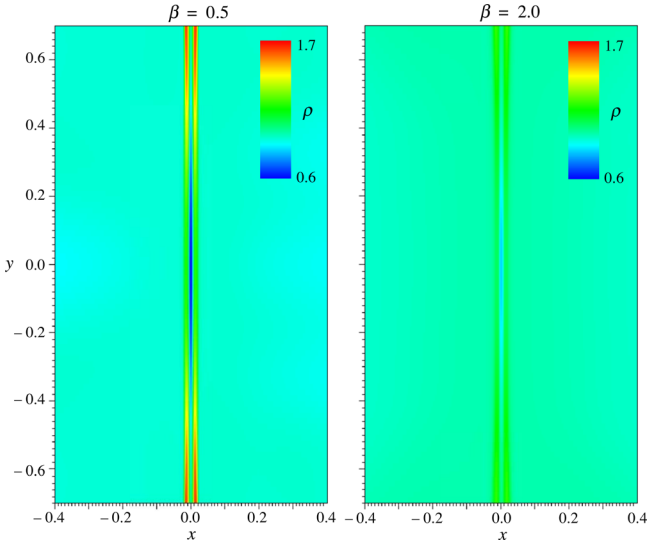

FIG. 6. A comparison of steady-state density distributions for low β (left) and high β (right) simulations using the Gaussian profile.

example).[32] The low density in the thin, internal layer leads to a more rapid acceleration of the plasma, so that both the density and the flow speed v_y have considerable variation within the layer as well as along it. Consequently, the theory's assumption that $\langle \rho v_y \rangle$ can be replaced by $\langle \rho \rangle \langle v_y \rangle$ becomes increasingly less valid as the plasma β decreases. The principal reason for the existence of a low-density layer within the diffusion region is the nonuniform distribution of current density across it. The current density concentrates towards the center of the diffusion region as the slow shocks approach one another (cf. Fig. 4), and this concentration leads to enhanced Ohmic heating and higher-temperature in the center. Since the total pressure is uniform, the mass density is necessarily lower within the high temperature region. Advection extends the high temperature and low density into the downstream region.

B. Petschek solutions for flat non-Gaussian resistivity profiles

We follow the same procedure as in Subsection IV A, using again $l_y = 0.3$ and $\eta_0 = 5 \times 10^{-4}$. First, at an early transient time ($t = 13$), a behavior that is clearly distinct from that obtained for the Gaussian profile can be clearly seen in Fig. 7. Indeed, the initial central point topology appears now to be unstable, with the formation of an O-point situated at the center of a small magnetic island (instead of an X-point). The slow-mode shocks that form are still present and are attached to the central island. The latter symmetric configuration is itself strongly unstable since the magnetic island quickly develops into a plasmoid, i.e., an island that is pushed and expelled on the negative y side as seen in Fig. 8 (at $t = 18$). Eventually, the system is able to evolve to a steady-state Petschek-like solution, as shown in Figs. 9 and 10. This new final state is clearly an asymmetric Petschek reconnection solution, since the diffusion region (see zoom in Fig. 10) is asymmetric along the y-direction with an X-point situated at $y = 0.18$. The four standing shocks remain, however, attached to the four tips of the diffusion layer as in a standard symmetric solution. The time evolution of the system is illustrated in Fig. 11, where the maximum current density J_{max} (obtained for a $x = 0$ cut) is plotted as a function of time. The result obtained for the previous Gaussian profile is also plotted for comparison. At early times, i.e., $t < 10$ time units, a symmetric Petschek solution is developing for both profiles in a similar way (J_{max} is increasing). However, at $t \approx 10$, a magnetic island appears at the center and grows in place until $t \approx 15$. During this second stage, symmetric slow-mode shocks envelop the island. At $t \approx 15$, the island begins to move and to be ejected as a plasmoid in one of the two y directions (negative y direction in this case according to Fig. 8). The plasmoid stage is characterized by two current density peaks embedding the moving island and coinciding with the two X-points, the highest peak being at the front. Finally, when the plasmoid is fully

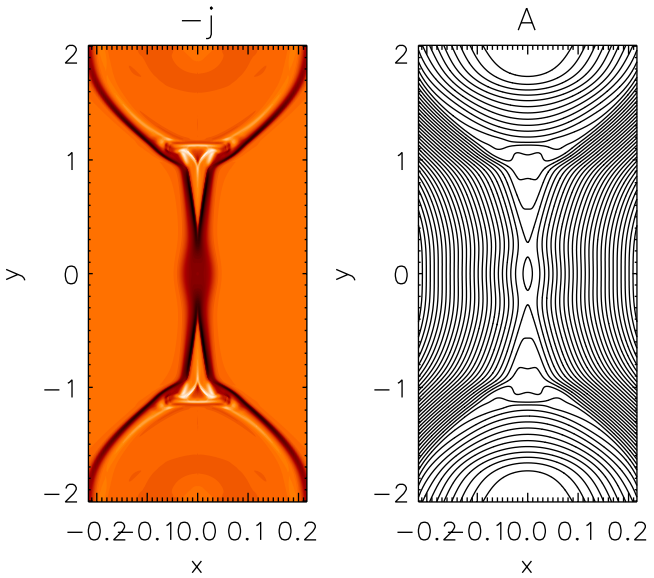

FIG. 7. Current density J (left panel) and magnetic field lines (right panel) for a transient state (at $t = 13$) for a simulation using $l_y = 0.3$ and a non-Gaussian resistivity profile corresponding to Eq. (10).

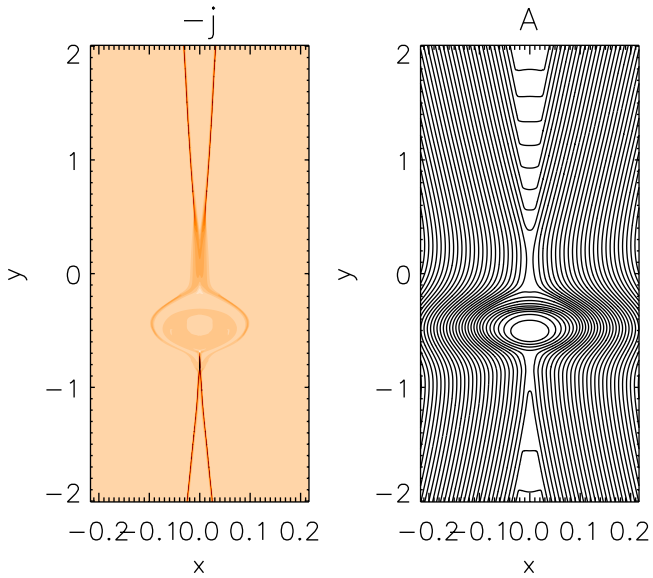

FIG. 8. Current density J (left panel) and magnetic field lines (right panel) for a transient state (at $t = 18$) for a simulation using $l_y = 0.3$ and a non-Gaussian resistivity profile corresponding to Eq. (10).

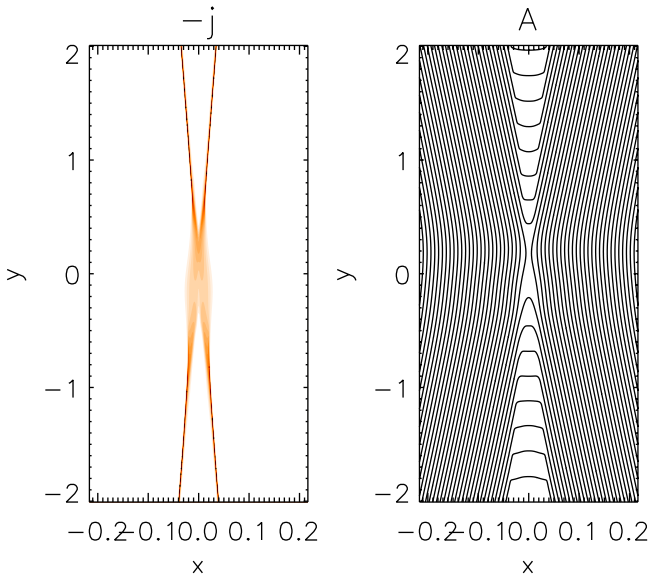

FIG. 9. Current density (J) and magnetic field lines for the final steady-state (at $t=40$) of the simulation using $l_y=0.3$ and a non-Gaussian resistivity profile corresponding to Eq. (10).

ejected at the external boundary, a steady state having an asymmetric Petschek solution is set up (see Fig. 10). One can note that the maximum current density is only very slightly higher than the value obtained for the similar Gaussian profile, reflecting a very similar reconnection rate.

An interesting question is what determines the half-plane location (positive y versus negative y half-plane) of the final X-point. We have run many simulations with different l_y values, and we found that the answer depends on the direction of the expelled plasmoid during the transient state. In fact, the X-point is located on the opposite side of the diffusion region from the plasmoid expulsion direction. Thus, when the plasmoid is ejected towards the negative y-direction, the final steady-state X-point forms on the positive y side (as shown previously) and vice versa. Moreover, running many cases leads to the conclusion that the direction is completely random, with the same number of positive and negative

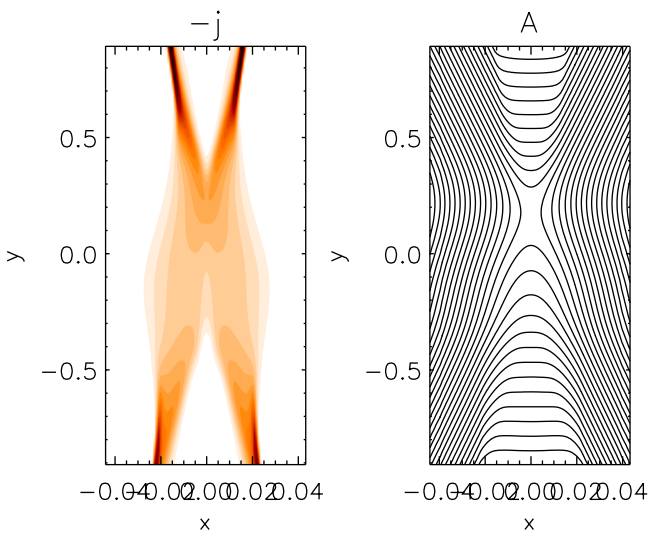

FIG. 10. Zoom of the previous figure.

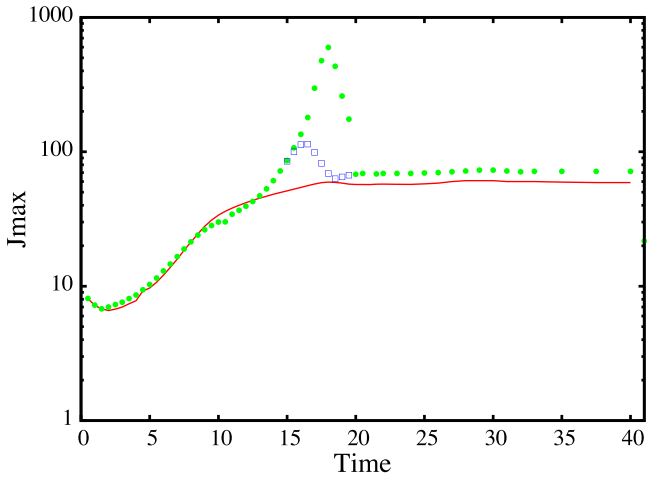

FIG. 11. Maximum current density J_{max} measured along the y direction (at $x=0$) as a function of time, for the Gaussian resistivity case (plain line), and non-Gaussian case (circles). The second maximum (second peak) for the non-Gaussian case is also plotted (with squares).

asymmetric X-point solutions. Moreover, we have checked that it is possible to enforce a given direction by prescribing a very small asymmetry in the resistivity profile with a magnitude that is slightly higher than the round-off errors.

The occurrence of two asymmetric solutions in a configuration that is otherwise symmetric is an example of spontaneous symmetry breaking. Such behavior is also predicted by the analytical theory when the resistivity profile is too flat to have a stable symmetric solution. For the non-Gaussian profile there are two stable, asymmetric solutions whose stagnation points are located about halfway between $y=0$ and $y=l_y$ (see Table II) in Sec. III. Each solution is similar to the numerical solution previously obtained by Baty *et al.* for an asymmetric resistivity profile of the form $\eta=\eta_c$ for $y<0$ and $\eta=\eta_c\exp(-y^2/l_y^2)$ for $y>0$.[11] Thus, the non-Gaussian profile $\eta=\eta_c\exp(-y^4/l_y^4)$ acts much like two displaced jumps with reverse orientations.

The asymmetric solutions are compared with the numerical solutions in Figure 12. The match between the numerical

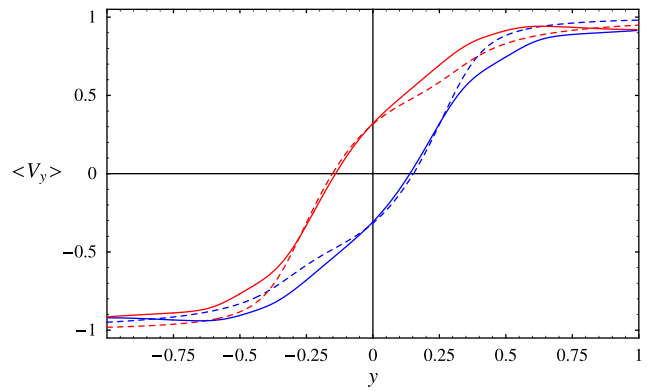

FIG. 12. Comparison of the averaged outflow velocity, $\langle v_y\rangle$ from the numerical simulation using a non-Gaussian resistivity profile (red and blue solid curves) with the corresponding flow predicted by the analytical theory (red and blue dashed curves). The blue simulation curve is for the run and time shown in Figures 9 and 10. The red simulation curve is for a separate run that uses the same initial conditions, except for small differences due to finite differencing and round-off errors.

and analytical solutions is not as quite as good as in the Gaussian case. There is still very good agreement within the diffusion region, but the agreement outside the diffusion region is not as good as before. Nevertheless, the percentage difference between the two is still less than the 20% error that often occurs with use of the one-dimensional nozzle equations.

The reconnection rate predicted by the analytical theory for the non-Gaussian profile is compared with the simulation values in Table III for $\beta = 0.35$ and $\beta = 10$, respectively. A difference of 13.7% occurs for the $\beta = 0.35$ case, but an error of only 0.5% occurs in the $\beta = 10$ case. In both cases, the predicted rate depends very weakly on the plasma β. Table IV compares the predicted location of the two stagnation points to the locations that occur in the simulations. The percentage differences are all less than 4%. The fact that the simulations values of $+0.152$ and -0.154 for $\beta = 10$ are not precisely anti-symmetric implies that there is a small numerical error of about 1.3% in this particular case. This error is probably due to the fact that the high β simulations exhibit small oscillations on the order of 1% in their final states. Such oscillations are not seen in the $\beta = 0.35$ case, so this case may provide more accurate steady-state values for both M_{Ai} and y_{sp}. From the perspective of the analytical theory, the $\beta = 10$ case is likely to be more accurate because of a reduced variation of ρ and v_y across the thickness of the outflow layer (see Figure 6).

C. Effect of l_y and resistivity on asymmetric Petschek reconnection

We have investigated the influence of the l_y parameter on the scenario of the formation of the asymmetric steady-state Petschek solution described above, when a flat non-Gaussian resistivity profile is imposed. The results are illustrated in Fig. 13 using J_{max} as a diagnostic tool. Three l_y values are employed, namely, 0.3, 0.2, and 0.1. Very similar behavior is then obtained for $l_y = 0.2$ and $l_y = 0.3$, with magnetic island formation in the center, followed by a plasmoid stage, and a final ejection just before settling into a steady state asymmetric configuration. This is, however, not the case for $l_y = 0.1$, where no plasmoid forms, despite again the appearance of a final asymmetric reconnection solution. Note also that the final steady-states exhibit higher current density (and higher corresponding reconnection rates) when l_y is smaller.

In order to explore the dependence with resistivity, an additional run employing a resistivity value that is twice the previous one is made, $\eta_0 = 10^{-3}$. The results are compared with the previous case (see Fig. 14). The initial growth rate

TABLE IV. Comparison of numerical and analytical stagnation point locations y_{sp}. (Simulation values are determined from center-line velocities at $x = 0$.)

η profile	β	Simulation	Theory	Difference (%)
Non-Gauss.	0.35	+0.157	+0.152	−3.2
Non-Gauss.	0.35	−0.157	−0.152	−3.2
Non-Gauss.	10	+0.152	+0.151	−0.7
Non-Gauss.	10	−0.154	−0.151	−1.9

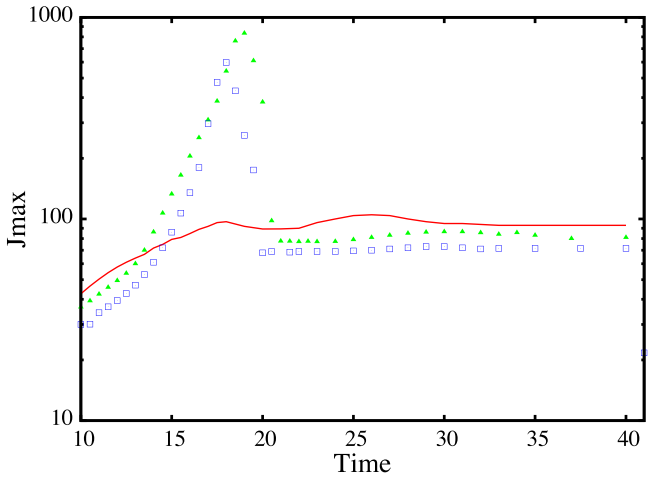

FIG. 13. Same as Fig. 11, for three runs using the non-Gaussian resistivity profile with $l_y = 0.1$ (plain line), $l_y = 0.2$ (triangles), and $l_y = 0.3$ (squares).

of the magnetic island appears to be very similar to the case with $\eta_0 = 5 \times 10^{-4}$, but the plasmoid ejection is faster.

D. Petschek solutions for mixed Gaussian/non-Gaussian resistivity profiles

It is instructive to study the effect of using a mixed (Gaussian and non-Gaussian y-components) resistivity profile, namely,

$$\eta(x,y) = \eta_0 \exp[-(x/l_x)^2 - [(y/l_4)^4 + (y/l_2)^2]/2], \quad (38)$$

with l_2 and l_4 defining the y Gaussian and non-Gaussian length contributions, respectively, which can now vary from case to case. We focus on a fixed maximum resistivity value with $\eta_0 = 5 \times 10^{-4}$.

Following the same procedure as previously described, we find that symmetric Petschek solutions are stable as long as l_2 is lower than l_4. The final steady-state is almost indistinguishable from a simulation with Gaussian profile with $l_y = 0.3$, the diffusion region characteristics and reconnection rate being very similar. In the opposite case ($l_4 < l_2$), the symmetric solution is unstable (in the same way as described

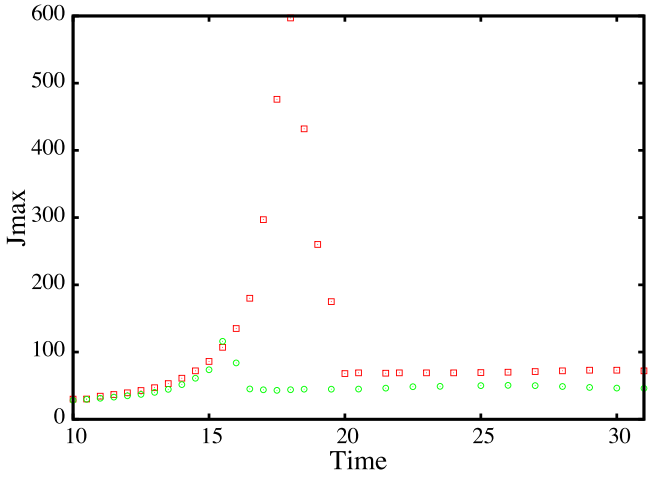

FIG. 14. Same as Fig. 11, for two runs using the non-Gaussian resistivity profile with $\eta_0 = 5 \times 10^{-4}$ (squares), and $\eta_0 = 1 \times 10^{-3}$ (circles).

in Subsection IV C) with the formation/ejection of a transient plasmoid. The final steady state is also dominated by an asymmetric Petschek solution.

This behavior is also predicted by the analytical theory. For $l_2/l_4 < 1.19$, the only stable solution is a symmetric one, but for $l_2/l_4 > 1.19$, the only stable solutions are the two asymmetric solutions lying on opposite sides of the symmetry axis. The transition of the symmetric solution from stable to unstable is not evident in the lowest order approximation based on setting V_3 and V_4 to zero (see Eqs. (29) and (30) in Sec. III). For $l_2/l_4 > 1.19$ these equations predict there are three solutions, one symmetric and the other two asymmetric. However, once $l_2/l_4 > 1.19$, the series expansion around $v_y = 0$ no longer converges, and only the expansions for the asymmetric solutions converge. Thus, the mere existence of a solution to (29) and (30) is not sufficient to guarantee that this solution is structurally stable. One also has to demonstrate that the series expansion of this solution is convergent.

V. DISCUSSION AND CONCLUSION

In this paper, we have investigated the stability of Petschek solutions for resistivity profiles that vary with distance along the length of the reconnection layer. We have also quantitatively compared our results to the theoretical analysis of Forbes *et al.*[5] This analysis predicts the rate of reconnection as measured by M_{Ai}, the Alfvén Mach number immediately upstream of the current layer at the location of the stagnation point, y_{sp}. For a Gaussian profile of the form $\exp(-y/l_y)^2$, we find that the reconnection rate predicted by the theory agrees with the simulation value to an accuracy of about 5% for a plasma β of 0.35 and about 8% for a plasma β of 10. These percentages are less than the 10%–20% error expected from the assumptions made by the analytical theory.[5,28]

For a non-Gaussian profile of the form $\exp(-y/l_y)^4$, the symmetric theory analysis predicts that there is no stable solution that is symmetric around $y = 0$. Here, we have extended the previously symmetric analysis to allow for asymmetric solutions. This asymmetric version of the theory predicts that there should be a stable asymmetric solution with a neutral point approximately located at either $+0.5l_y$ or $-0.5l_y$. Either solution is equally likely, but only one solution can occur at a time. In other words, the symmetry of the system is spontaneously broken. The numerical simulations confirm this behavior. Which solution occurs in the numerical simulations depends upon small, random fluctuations in the initial conditions. In the asymmetric solutions, the discrepancy between the theoretical and numerical reconnection rates is about 14% for $\beta = 0.35$, but only 1% for $\beta = 10$. The predicted locations of the stagnation points (approximately the same as the location of the neutral points) is confirmed to an accuracy of about 3% and 2% for $\beta = 0.35$ and $\beta = 10$, respectively.

The effect of compressibility on the reconnection rate, as measured by M_{Ai}, is relatively weak. The analytical theory predicts that the reconnection rate should decrease by about 2% as β varies from 0.35 to 10, but the simulations actually show an increase of about 10%. We attribute this discrepancy between the simulation and theory values to the fact that the theory ignores the variation in density across the width of the current layer. This variation increases as the system becomes more compressible with decreasing β.

For both the symmetric and asymmetric solutions, the length of the diffusion region is roughly equal to l_y, the length scale over which the resistivity varies. Also for both solutions, the reconnection rate, M_{Ai}, is roughly $Lu_{ly}{}^{-1/2}$, where Lu_{ly} is the Lundquist number based on the scale length l_y. Although the neutral and stagnation points are not collocated in general, the separation between them is very small (of order M_{Ai}^2). Thus, both the neutral point and the stagnation point lie at nearly the same location. This location depends strongly on the functional form of the resistivity profile, and it typically occurs next to a region where the profile has a steep gradient.

In most of our simulations, asymmetric solutions are obtained by the formation and ejection of a plasmoid. Thus, it is tempting to try to relate this process to the plasmoid instability, which develops in a reconnecting Sweet-Parker current layer when the local Lundquist number exceeds a value on the order 10^4.[39] However, the local Lundquist number just prior to plasmoid formation in our simulations is estimated to be less than 10^3. Since the theory developed here assumes a laminar flow, it does not incorporate the physics of such instabilities. It could be interesting, therefore, in a future study to explore more deeply the dependence with resistivity in order to understand better the criterion for spontaneous symmetry breaking and to compare it with plasmoid instability.

Our results may have relevance to reconnection in the lower solar atmosphere. The resistivity of the plasma changes dramatically at the thin interface (transition zone) separating the chromosphere from the corona and also at the interface separating the photosphere from the chromosphere.[33] Any current sheet intersecting these interface regions might, therefore, be expected to undergo rapid reconnection. The reconnection rate would be determined by the thickness of the interface. Such reconnection might be significant for coronal heating,[34] photospheric flux cancellation,[35] or spicule generation.[36,37]

There are several important questions that have yet to be answered: What aspects of the behavior we find in the resistive MHD equations carry over into the kinetic plasma regimes? For example, does the ion-inertial length in Hall-MHD play the same role as the scale, l_y, of the resistivity variation? What are the effects of boundary conditions, both in the inflow and in the outflow regions? Petschek reconnection is undriven, so what happens if the inflow is driven, or the outflow is blocked? Finally, our theoretical analysis assumes the flow is laminar, but in many applications the flow is expected to be turbulent. How much, if any, of the behavior observed in the laminar regime carries over in the turbulent regime?[38]

ACKNOWLEDGMENTS

The numerical simulations in this work have been performed using the Verstatile Advection Code maintained by G. Toth and R. Keppens (http://grid.engin.umich.edu/~gtoth/VAC/). E. R. Priest is grateful to the Leverhulme

Trust. T. G. Forbes received support from NASA grant NNX-10AC04G to the University of New Hampshire. H. Baty acknowledges support by French National Research Agency (ANR) through Grant ANR-13-JS05-0003-01 (Project EMPERE). We also acknowledge computational facilities available at Equip@Meso of the Université de Strasbourg. Finally, we sincerely thank the referee for useful suggestions that helped improve the content of the paper.

[1]E. R. Priest and T. G. Forbes, *Magnetic Reconnection* (Cambridge University Press, 2000).
[2]P. A. Sweet, in *Electromagnetic Phenomena in Cosmic Physics*, edited by B. Lenhert (Cambridge University Press, 1958), p. 135.
[3]E. N. Parker, J. Geophys. Res. **62**, 509, doi:10.1029/JZ062i004p00509 (1957).
[4]H. E. Petschek, in *The Physics of Solar Flares*, edited by W. N. Hess (NASA, SP-50, 1964), p. 425.
[5]T. G. Forbes, E. R. Priest, D. B. Seaton, and Y. E. Litvinenko, Phys. Plasmas **20**, 052902 (2013).
[6]G. Tóth, Astrophys. Lett. Commun. **34**, 245 (1996).
[7]P. Collela and P. R. Woodward, J. Comput. Phys. **54**, 174 (1984).
[8]A. Harten, J. Comput. Phys. **49**, 357 (1983).
[9]R. B. Brackbill and D. C. Barnes, J. Comput. Phys. **35**, 426 (1980).
[10]H. Baty, E. R. Priest, and T. G. Forbes, Phys. Plasmas **13**, 022312 (2006).
[11]H. Baty, T. G. Forbes, and E. R. Priest, Phys. Plasmas **16**, 012102 (2009).
[12]H. Baty, E. R. Priest, and T. G. Forbes, Phys. Plasmas **16**, 060701 (2009).
[13]T. G. Forbes, Earth Planets Space **53**, 423 (2001).
[14]H. Baty, Phys. Plasmas **19**, 092110 (2012).
[15]V. M. Vasyliunas, Rev. Geophys. **13**, 303, doi:10.1029/RG013i001p00303 (1975).
[16]V. S. Titov, in *Physics of Solar Flares*, edited by B. V. Somov (IZMIRAN, Moscow, 1985), p. 141.
[17]B. V. Somov, *Physical Processes in Solar Flares* (Kluwer, Dordrecht, 1992), p. 249.
[18]R. D. Blandford and M. J. Rees, MNRAS **169**, 395 (1974).
[19]S.-H. Kim and A. C. Raga, Astrophys. J. **379**, 689 (1991).
[20]K. Liffman, Publ. Astron. Soc. Aust. **18**, 267 (2001).
[21]L. M. Malyshkin, L. M. T. Linde, and R. M. Kulsrud, Phys. Plasmas **12**, 102902 (2005).
[22]R. M. Kulsrud, Phys. Plasmas **18**, 111201 (2011).
[23]D. B. Seaton and T. G. Forbes, Astrophys. J. **701**, 348 (2009).
[24]E. R. Priest and T. G. Forbes, J. Geophys. Res. **91**, 5579, doi:10.1029/JA091iA05p05579 (1986).
[25]L. M. Malyshkin and R. M. Kulsrud, Phys. Scr. **T142**, 014034 (2010).
[26]R. M. Green, in *Solar and Stellar Magnetic fields*, edited by R. Lüst (North-Holland Publishing Co., Amsterdam, 1965), p. 398.
[27]S. I. Syrovatskii, Sov. Phys. JETP **33**, 933 (1971).
[28]S. Schreier, *Compressible Flow* (Wiley, New York, 1982), p. 577.
[29]S. Zenitani and T. Miyoshi, Phys. Plasmas **18**, 022105 (2011).
[30]M. Scholer, J. Geophys. Res. **94**, 8805, doi:10.1029/JA094iA07p08805 (1989).
[31]M. Yan, L. C. Lee, and E. R. Priest, J. Geophys. Res. **97**, 8277, doi:10.1029/92JA00170 (1992).
[32]T. Yokoyama and K. Shibata, Astrophys. J. **549**, 1160 (2001).
[33]J. Kubat and M. Karlicky, "Electrical conductivity in the solar photosphere and chromosphere," Bull. Astron. Inst. Czech. **37**(3), 155–163 (1986).
[34]A. F. Rappazzo, M. Velli, G. Einaudi, and R. B. Dahlburg, Astrophys. J. **677**, 1348 (2008).
[35]A. Takeuchi and K. Shibata, Earth Planets Space **53**, 605 (2001).
[36]S. Koutchmy, B. Filippov, and E. Tavabi, "About the magnetic origin of chromospheric spicules and coronal jets," EAS Publ. Ser. **55**, 257 (2012).
[37]J. E. Leake, V. S. Lukin, and M. G. Linton, Phys. Plasmas **20**, 061202 (2013).
[38]Y.-M. Huang and A. Bhattacharjee, Phys. Plasmas **17**, 062104 (2010).
[39]N. F. Loureiro, A. A. Schekochihin, and D. A. Uzdensky, Phys. Rev. E **87**, 013102 (2013).